Chemical Science

Accepted Manuscript

This article can be cited before page numbers have been issued, to do this please use: L. Kong, Z. Chen, Y. Chen, L. Wang, Y. Wang and Y. Li, *Chem. Sci.*, 2026, DOI: 10.1039/D6SC03277J.

ROYAL SOCIETY OF CHEMISTRY

rsc.li/chemical-science

View Article Online
DOI: 10.1039/D6SC03277J

ARTICLE

Cation Concentration-Dependent Reaction Kinetics in Single-Atom Catalysts for Electrochemical CO_2 Reduction

Received 00th January 20xx,
Accepted 00th January 20xx

DOI: 10.1039/x0xx00000x

Lingyi Kong,[a] Zhe Chen,[a] Yuheng Chen,[a] Lingxiao Wang,*[,a] Yu Wang[a] and Yafei Li*[,a]

Electrolyte cations are widely recognized as critical promoters in electrochemical CO_2 reduction reaction (CO_2RR), yet the field has largely focused on cation identity while overlooking a more fundamental and practical parameter, namely cation concentration. Whether increasing cation concentration continuously enhances catalytic activity remains an open and consequential question, and the lack of mechanistic understanding has limited the rational design of electrolyte environments. Here, we demonstrate that cation concentration is not merely a secondary parameter, but a decisive kinetic regulator that fundamentally governs CO_2RR performance. By integrating constant-potential ab initio molecular dynamics simulations with experiments, we reveal a previously unrecognized nonmonotonic ("volcano-type") dependence of catalytic activity on K^+ concentration over Ni-N-C single-atom catalysts. At moderate concentrations, K^+ promotes CO_2 activation by restructuring the interfacial hydrogen-bond network and stabilizing key intermediates. Strikingly, further increasing K^+ concentration leads to over-stabilization of *CO, impeding its desorption and suppressing overall reaction rates. This "double-edged" effect establishes an intrinsic trade-off between intermediate activation and product release. Experimental measurements directly validate this prediction, exhibiting a pronounced rise-and-fall trend in CO partial current density.

Introduction

Electrochemical carbon dioxide reduction reaction (CO_2RR) is a promising technology that can convert electricity generated from renewable energy sources into carbon-based fuels and chemicals for storage.[1,2] This carbon-negative process involves multiple proton-coupled electron transfer steps and can yield a variety of reduction products (*e.g.*, CO, CH_4, C_2H_4, and EtOH) when facilitated by efficient electrocatalysts.[3,4] Although multi-electron products, particularly C_{2+} species, possess higher commercial value, to date only Cu-based catalysts have demonstrated the capability to drive multi-electron CO_2 reduction,[5] albeit with limited product selectivity and low energy conversion efficiency. In contrast, the conversion of CO_2 to carbon monoxide (CO) via a simple two-electron ($2e^-$) pathway offers higher selectivity and energy efficiency, rendering it a more practical route for industrial-scale CO_2RR.[6]

In this context, silver and gold are widely regarded as promising catalysts of CO production owing to their appreciable activity and selectivity,[7] however, the intrinsically high cost of these noble metals severely limits their large-scale application in CO_2RR. Recently, low-cost single-atom catalysts (SACs) have attracted considerable attention as promising alternatives to noble-metal catalysts for CO_2RR, owing to their maximal atom utilization and well-defined active sites.[6,8] Among various SACs, nickel-nitrogen-carbon (Ni-N-C) SACs featuring NiN_4 moieties have been extensively studied because of their high selectivity toward the 2e-CO_2RR.[9,10] For instance, Li et al. reported that Ni-N-C SACs can achieve near-unity CO selectivity with the current density of 28.6 mA cm^{-2} at −0.81 V_{RHE} in CO_2-saturated 0.5 M $KHCO_3$.[11] Similarly, Liu and co-workers designed atomically dispersed Ni on nitrogenated graphene as an efficient electrocatalyst for CO_2 reduction to CO, which shows a Faradaic efficiency (FE) of 97% and a current density of 22 mA cm^{-2} at a mild overpotential of 0.61 V.[12] Despite their excellent selectivity, the relatively low current densities of Ni-N-C SACs remain insufficient for commercial applications, indicating substantial room for improving the kinetics of CO_2RR on these catalysts.

In recent years, the influence of metal cations (e.g. K^+, Na^+, Li^+, etc.) on the thermodynamics and kinetics of electrochemical CO_2RR has emerged as an important research focus.[13-16] Metal cations are generally recognized to modulate the hydrogen-bond network of water molecules, the electric field at the electrochemical double layer, and the local electronic structure of the catalyst, thereby influencing the adsorption of key intermediates and product selectivity of CO_2RR.[17-22] Wu *et al*. reported that in the absence of metal cations, the CO_2RR on Ni-N-C SACs is even shut down while the hydrogen evolution reaction (HER) becomes the dominant reaction, underscoring the essential role of metal cations in initiating CO_2RR.[23] Although the importance of metal cations has been well established, most previous studies have focused primarily on the effects of cation identity (i.e., ionic radius), whereas another crucial parameter, cation concentration, has received comparatively limited attention. Recently, several studies have shown that increasing the K^+ concentration can further enhance the current density of Ni-N-C SACs for CO_2-to-CO conversion, offering a new avenue for improving catalytic performance.[23-25] However, the underlying mechanisms by

[a]Jiangsu Collaborative Innovation Center of Biomedical Functional Materials, Jiangsu Key Laboratory of New Power Batteries, School of Chemistry and Materials Science, Nanjing Normal University, Nanjing 210023, China.
Email: lxwang46@nnu.edu.cn (LW) and liyafei@njnu.edu.cn (YL)
† Supplementary Information (SI) available. See DOI: 10.1039/x0xx00000x

which elevated cation concentrations influence the thermodynamics and kinetics of CO_2RR remain unclear. More fundamentally, it is still unresolved whether the activity of Ni-N-C SACs continues to improve monotonically with increasing cation concentration. Addressing these questions is essential for advancing the practical application of Ni-N-C SACs in CO_2RR and for achieving optimal catalytic performance through rational electrolyte design.

In this work, we employed constant-potential *ab initio* molecular dynamics (AIMD) simulations in conjunction with a hybrid solvent model containing varying concentrations of potassium cations (K^+) to systematically investigate the effect of cation concentration on the CO_2RR performance of Ni-N-C SACs. Potassium ion (K^+) was selected as the representative cation because potassium salts (e.g. KCl, $KHCO_3$) are the most commonly used electrolytes in experimental studies. Our theoretical results reveal that increasing K^+ concentration progressively disrupts the hydrogen-bond network of interfacial water and strengthens the interaction between CO_2 and the Ni active center, thereby accelerating the kinetics of CO_2 reduction to CO. However, at high K^+ concentrations, the interaction between Ni active center and the reaction product *CO is significantly enhanced, leading to an increase in the kinetic barrier for *CO desorption, suggesting that the overall reaction kinetics do not necessarily improve with increasing cation concentration. Consistent with these theoretical insights, our experimental measurements demonstrate that the partial current density of Ni-N-C SACs for CO_2-to-CO conversion does not increase monotonically with cation concentration, instead reaching an optimum at intermediate K^+ levels.

Results and discussion

Concentration Effect of K^+ on CO_2 Adsorption and Activation.

Structurally, Ni-N-C SACs predominantly feature two distinct NiN_4 moieties according to different types of coordinating N atoms, namely pyridinic and pyrrolic N. Experimental studies have demonstrated that Ni-N-C SACs comprising pyridinic- and pyrrolic-type NiN_4 both exhibit appreciable catalytic activity toward CO_2RR.[26-28] However, the contribution of the pyridinic-type NiN_4 to CO_2RR activity is still a matter of debate, as evidenced by the calculated thermodynamic barrier of 1.5 eV for the first elementary step of CO_2 hydrogenation.[11] This is likely attributable to substantial differences between the idealized pyridinic-type NiN_4 models employed in theoretical simulations and the actual structures present in experiments. Consequently, elucidating the true active-site structure of pyridinic-type NiN_4 has become a subject of ongoing theoretical investigations,[29-31] although it is beyond the scope of the present

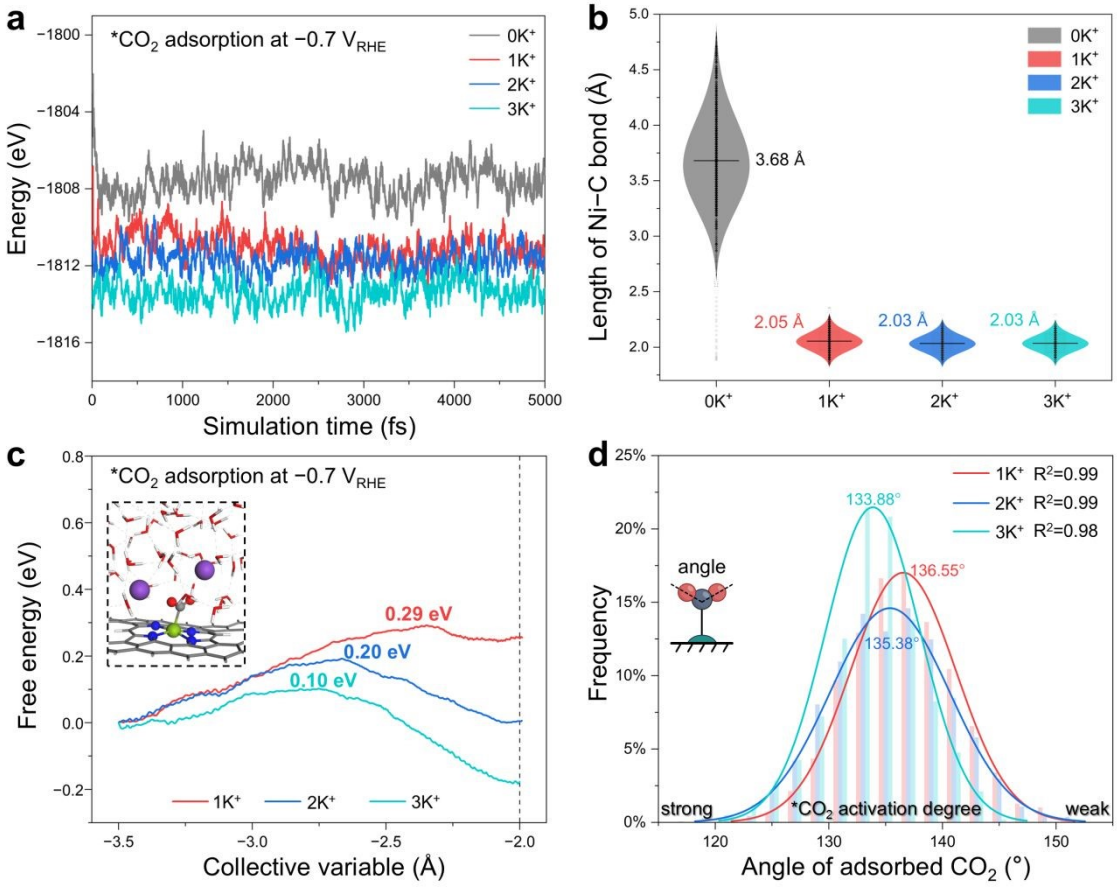

Fig. 1 Variations of energy (a) and Ni-C bond length (b) against the time during the constant-potential AIMD simulations for CO_2 adsorption on Ni-N-C SACs at −0.7 V_{RHE}. (c) Free energy profiles for CO_2 adsorption over Ni-N-C SACs under different K^+ conditions. (d) Statistical analysis for the distribution of the angle of adsorbed $^*CO_2$ under three K^+ conditions.

View Article Online
DOI: 10.1039/D6SC03277J

work. In contrast, prior theoretical studies have consistently shown that the pyrrolic-type NiN_4 moiety exhibits favorable catalytic activity for CO_2RR.[32] Accordingly, pyrrolic-type NiN_4 (Fig. S1) is adopted here as a more appropriate than pyridinic-type NiN_4 as the theoretical active center structure of Ni-N-C SACs for investigating the relationship between CO_2 reduction and cation concentration.

Stable adsorption and effective activation of CO_2 on the catalyst surface are essential prerequisites for efficient CO_2RR. Accordingly, constant-potential AIMD simulations were performed to investigate CO_2 adsorption on Ni-N-C SACs at different K^+ concentrations under pH 6.8 and an applied potential of −0.7 V_{RHE}, consistent with experimental conditions.[9-11] Four K^+ concentrations were considered by introducing 0, 1, 2, or 3 K atoms into the supercell (Fig. S1). The introduced K atoms were ionized into K^+ through electron transfer to the catalyst surface. Note that the $3K^+$ condition modeled here is close to a K^+ concentration of 2 M, as used by Wu *et al*. in their experiments.[23] As shown in Fig. 1a, CO_2 adsorption in all four solvent environments ($0K^+$, $1K^+$, $2K^+$, and $3K^+$) reached energetic equilibrium within 5 ps AIMD simulations. Notably, in the $0K^+$ condition, CO_2 could not be stably adsorbed and tended to diffuse back into the solvent, as evidenced by a persistent Ni-C distance greater than 3 Å. Our AIMD simulations achieve good agreements with experiment observations that Ni-N-C SACs is inactive for CO_2RR in the absence of K^+. In sharp contrast, upon introducing K^+, irrespective of concentration, the Ni-C bond length fluctuated around ~2 Å (Fig. 1b), indicating the formation of a chemical bond between CO_2 and the Ni active site. These results demonstrate that K^+ plays a crucial role in facilitating CO_2 adsorption.

To evaluate the effect of K^+ concentration, we then calculated the free-energy profiles for CO_2 adsorption ($* + CO_2(g) \rightarrow *CO_2$) using constrained constant-potential AIMD simulations with a slow-growth approach. As shown in Fig. 1c (more details can be found in Fig. S2−S4), the free-energy barrier for CO_2 adsorption on Ni-N-C SACs decreases progressively with increasing K^+ concentration, reaching 0.29, 0.20, and 0.10 eV under $1K^+$, $2K^+$, and $3K^+$ conditions, respectively. Remarkably, the adsorption process is endothermic under $1K^+$ conditions, but it becomes exothermic when the K^+ concentration increases to $2K^+$ and $3K^+$. In contrast, when the adsorption configuration involves the O atom bonded to the Ni site, (i.e., OCO adsorption), negligible cation effects can be observed, with the free energy barriers > 0.80 eV (Fig. S5). This indicates that the OCO adsorption configuration is independent of cation concentration and energetically unfavorable.

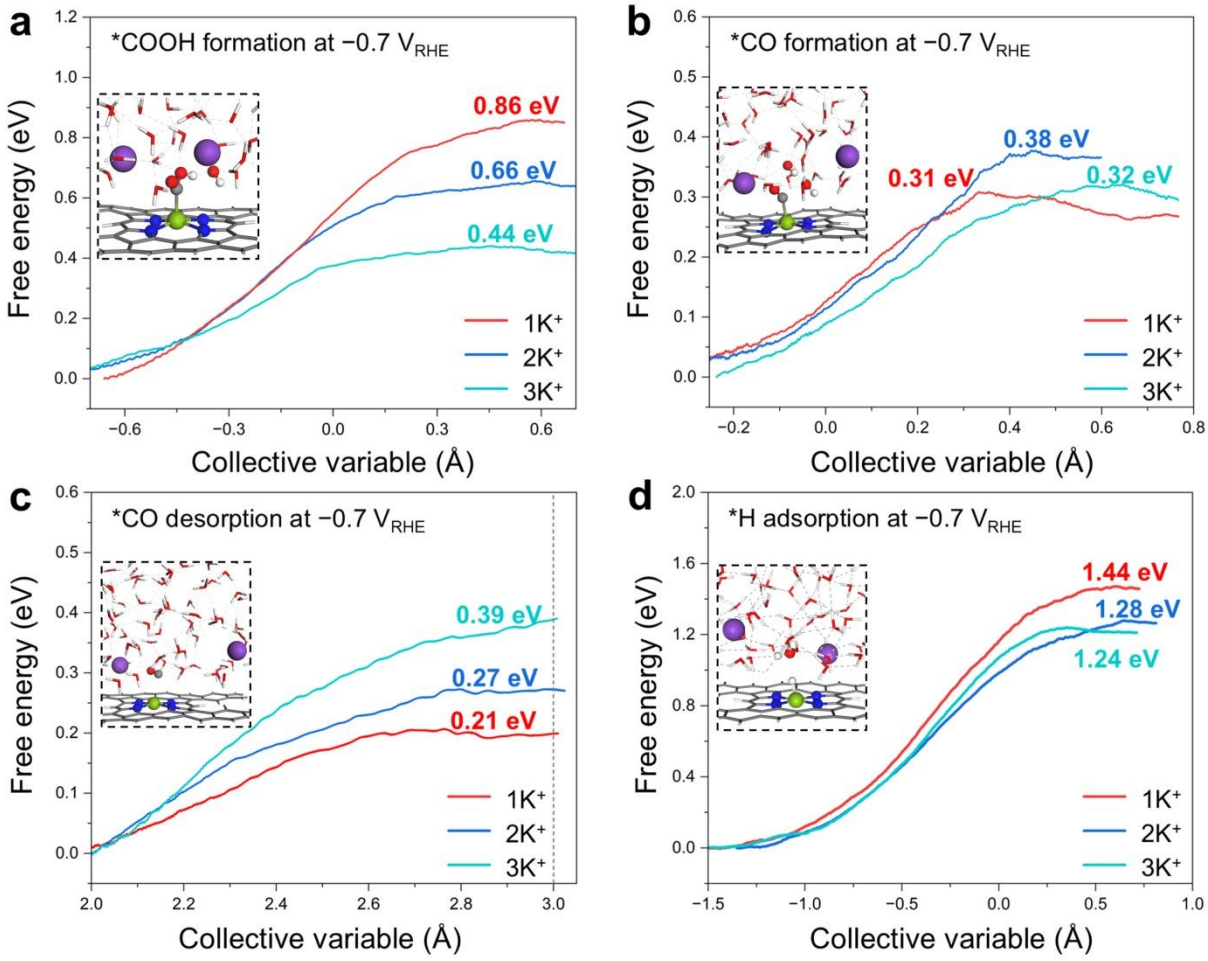

Fig. 2 Free energy profiles for (a) *COOH formation, (b) *CO formation, (c) CO desorption and (d) *H adsorption on Ni-N-C SACs under different K^+ conditions.

View Article Online
DOI: 10.1039/D5SC07277J

To evaluate the degree of CO_2 activation, we further analyzed the bending angle distribution of $*CO_2$ obtained from AIMD trajectories. As shown in Fig. 1d, the most probable bending angle decreases from 136.55° at $1K^+$ to 135.38° at $2K^+$ and further to 133.88° at $3K^+$. Because a greater deviation from the linear 180° geometry corresponds to stronger activation, these results indicate enhanced CO_2 activation at higher K^+ concentrations. Meanwhile, increasing the K^+ concentration leads to a gradual elongation of the total C–O bond, accompanied by a shortening of the Ni–C bond (Fig. S6). Overall, increasing K^+ concentration improves both the kinetics and thermodynamics of CO_2 adsorption and promotes CO_2 activation, thereby facilitating subsequent CO_2 reduction.

Concentration Effect of K^+ on CO_2 Reduction.

Mechanistically, adsorbed $*CO_2$ undergoes two proton-coupled electron transfer (PCET) steps to form CO, with the first PCET step corresponding to the hydrogenation of $*CO_2$ to *COOH generally recognized as the rate-determining step of CO_2RR.[26-30] To elucidate the effect of cation concentration on this critical step, we investigated the reaction kinetics for the hydrogenation process of $*CO_2$ ($*CO_2 + H_2O + e^- \rightarrow *COOH + OH^-$) under different K^+ concentrations. As shown in Fig. 2a (more details can be found in Fig. S7–S9), under the $1K^+$ condition, the hydrogenation of $*CO_2$ exhibits a relatively high free-energy barrier of 0.86 eV at −0.7 V_{RHE}, indicating sluggish kinetics and a substantial obstacle to CO_2RR. Notably, this barrier decreases to 0.66 and 0.44 eV under $2K^+$ and $3K^+$ conditions, respectively, demonstrating that increasing K^+ concentration significantly facilitates *COOH formation. Moreover, statistical analysis of AIMD trajectories reveals a progressive shortening of the Ni-C bond length with increasing cation concentration (Fig. S10). This trend indicates that higher K^+ concentrations strengthen the interaction between the *COOH intermediate and the Ni active center, thereby facilitating the reaction kinetics.

Subsequently, the second PCET step, corresponding to the conversion of *COOH to adsorbed *CO ($*COOH + e^- \rightarrow *CO + OH^-$) on Ni-N-C SACs, was investigated at −0.7 V_{RHE} under different K^+ concentrations. As shown in Fig. 2b and Fig. S11–S13, the free-energy

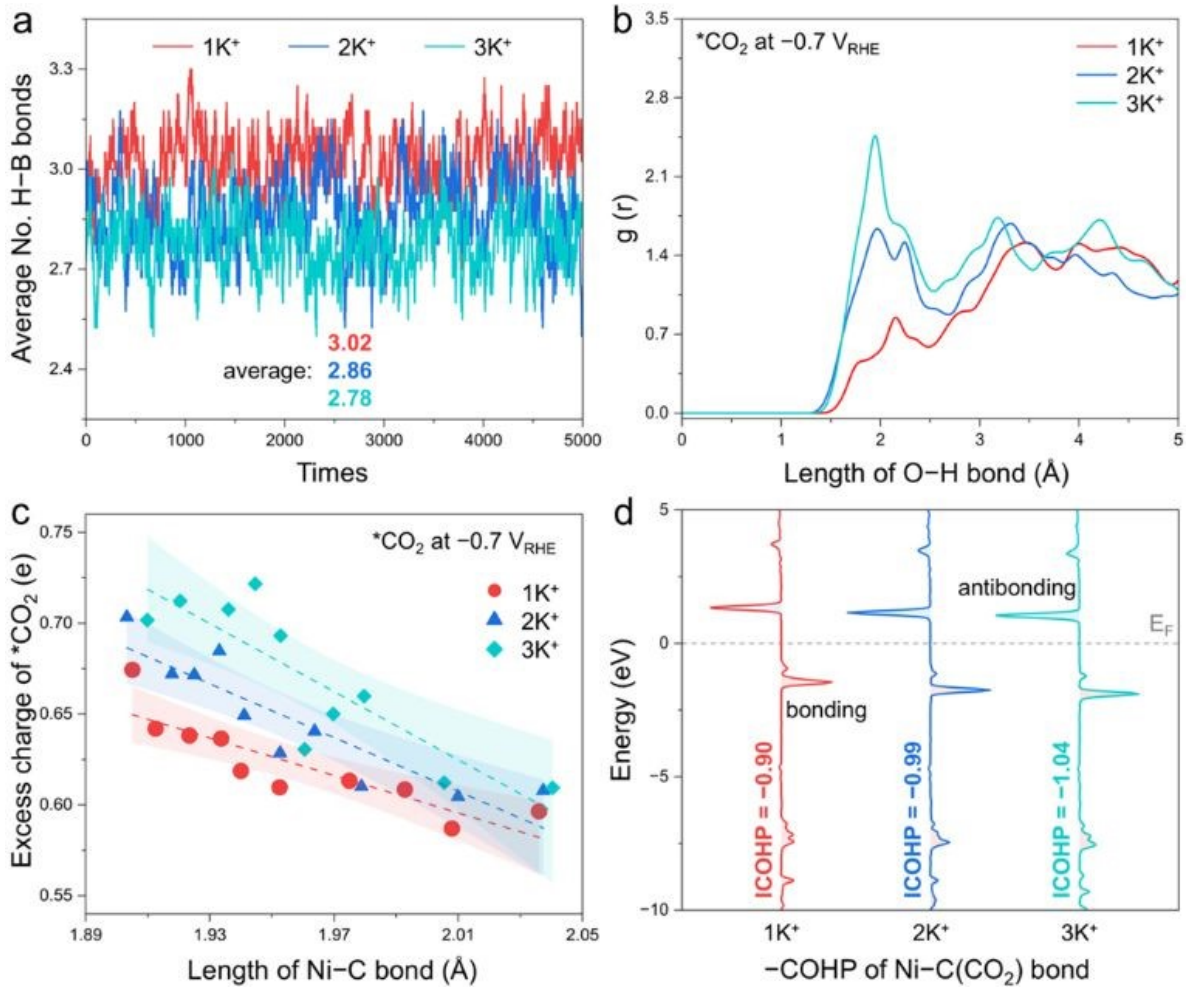

Fig. 3 (a) Average number of hydrogen bonds in explicit H_2O during the AIMD simulation trajectories under different K^+ conditions. (b) Radial distribution function of $^*CO_2$ toward H atoms in the explicit solvent. (c) Correlation between the Ni-C bond lengths and the excess charge of $^*CO_2$ for multiple random configurations at three K^+ conditions. (d) COHP analysis of the Ni-C ($^*CO_2$) bond under different K^+ conditions. The Fermi level (E_F) was set to zero, with bonding and antibonding states shown on the right and left, respectively.

View Article Online
DOI: 10.1039/D5SC03775J

barriers for this step are minimally affected by cation concentration, with values of 0.31, 0.38, and 0.32 eV for $1K^+$, $2K^+$, and $3K^+$, respectively. These relatively low barriers indicate facile *CO formation, confirming that this step is not rate-limiting and is largely insensitive to K^+ concentration. The generated *CO must subsequently desorb from the Ni active site to release gaseous CO and regenerate the catalyst for the next CO_2RR cycle. As presented in Fig. 2c and Fig. S14−S16, the calculated free-energy barriers for *CO desorption at −0.7 V_{RHE} are 0.21, 0.27, and 0.39 eV for eV $1K^+$, $2K^+$, and $3K^+$ conditions, respectively. These results reveal that *CO desorption becomes progressively less favorable as cation concentration increases. Nevertheless, even under the $3K^+$ condition, the barrier remains sufficiently low to sustain efficient CO production. Overall, the presence of K^+ stabilizes CO_2 adsorption and significantly enhances CO_2RR kinetics by lowering the energy barrier of the rate-determining *COOH formation step, although excessive cation concentration begins to impede *CO desorption.

In addition to CO_2RR on Ni-N-C SACs, the competitive HER must be considered to evaluate catalytic selectivity under different K^+ concentrations. Specifically, the PCET processes may occur either on adsorbed $*CO_2$, leading to CO_2 conversion, or directly on the Ni active center, resulting in competitive H_2 generation. To assess this competition, we calculated the free-energy barrier of the Volmer step ($*H_2O + e^- \rightarrow *H + OH^-$) on the Ni active center at varying K^+ concentrations (Fig. 2d and Fig. S17−S19). Constrained AIMD simulations at −0.7 V_{RHE} reveal a slightly decreasing yet consistently high free-energy barrier (> 1.2 eV) for the Volmer step as K^+ concentration increases. Notably, these barriers are substantially higher than those associated with CO_2 adsorption and reduction, indicating that the Ni active center effectively suppresses HER and thus maintains high catalytic selectivity for CO_2RR at −0.7 V_{RHE}. To ensure the accuracy of the kinetic descriptions of key steps in CO_2RR, multiple independent constrained AIMD simulations were performed (Fig. S20). Indeed, negligible error fluctuations can be observed, which ensures the reliability of our theoretical results and mechanistic conclusions.

Origin of Cation Concentration Effect on CO_2RR.

Understanding the role of cation concentration from the perspective of the interfacial microenvironment and electronic structure is essential for optimizing catalytic performance beyond the intrinsic properties of active sites. As shown in Fig. 3a and Fig. S21, we first examined the effect of K^+ concentration on the interfacial microenvironment in the absence of CO_2. The results indicate that the average number of hydrogen bonds of each explicit H_2O molecule decreases progressively with increasing K^+ concentration, being 3.02, 2.86, and 2.78 for $1K^+$, $2K^+$, and $3K^+$ conditions, respectively. This disruption of the hydrogen-bond network facilitates the transport of CO_2 through the solvent, enabling easier access to the Ni active centers. In addition, K^+ concentration markedly influences the spatial orientation of interfacial H_2O molecules (Fig. S22). Under the $1K^+$ condition, most interfacial water molecules adopt an "O-down" configuration, whereas at $2K^+$ and $3K^+$ concentrations, a greater proportion of H_2O molecules exhibit an "H-down" orientation. Correspondingly, the shortest distance between adsorbed CO_2 and the hydrogen atoms of interfacial H_2O decreases with increasing cation concentration (Fig. 3b). The prevalence of the "H-down" configuration promotes CO_2 hydrogenation by shortening the proton-transfer distance, thereby lowering the kinetic barrier for CO_2 hydrogenation under high-cation-concentration conditions.

The promotional effect of K^+ concentration on CO_2RR can also be elucidated from an electronic-structure perspective. Across the three K^+ concentrations, a clear correlation is observed between the Ni-C bond length and the excess charge on the adsorbed $*CO_2$ species (Fig. 3c). Under the $1K^+$ condition, as the Ni-C bond length varies from 1.90 to 2.04 Å, the charge transferred to $*CO_2$ ranges from 0.59 to 0.67 e. In contrast, under $2K^+$ and $3K^+$ conditions, $*CO_2$ gains a relatively larger amount of charge (0.61−0.72 e) from the catalyst. The increased charge transfer strengthens the interaction between $*CO_2$ and the positively polarized Ni active center, thereby enhancing CO_2 adsorption and activation. Besides, the d_{z2} orbitals of Ni site gradually approach the Fermi level with cation concentration (Fig. S23), becoming more active occupied orbitals. After CO_2 adsorption, these occupied orbitals disappear significantly, while new bonding orbitals emerge at positions far below the Fermi level, which suggests the formation of more stable chemical bonds.

To further quantify the Ni-$*CO_2$ interaction at different K^+ concentrations, we performed crystal orbital Hamilton population (COHP) analysis. A more negative integrated COHP (ICOHP) value corresponds to a stronger chemical bond. As shown in Fig. 3d, the number of bonding states below the Fermi level increases with rising K^+ concentration. Consequently, the ICOHP value of the Ni-C bond shifts toward more negative values as cation concentration increases, indicating progressively strengthened catalyst-adsorbate interactions.

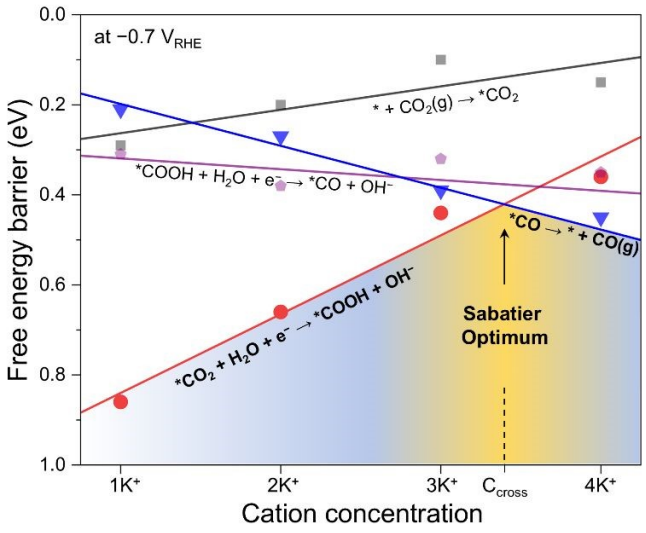

Fig. 4 Free energy barriers for each elementary step in the CO_2RR pathway on Ni-N-C SACs at different K^+ conditions.

Theoretical Prediction of the Existence of an Optimal Cation Concentration.

The above DFT calculations, based on a systematic analysis of cation-concentration-dependent reaction pathways and kinetic responses, demonstrate the positive role of K^+ in promoting CO_2RR on Ni-N-C SACs. However, an important question remains: does continuously increasing K^+ concentration always enhance CO_2RR kinetics before the electrolyte reaches saturation? Indeed, we have found that the

View Article Online
DOI: 10.1039/D6SC03277J

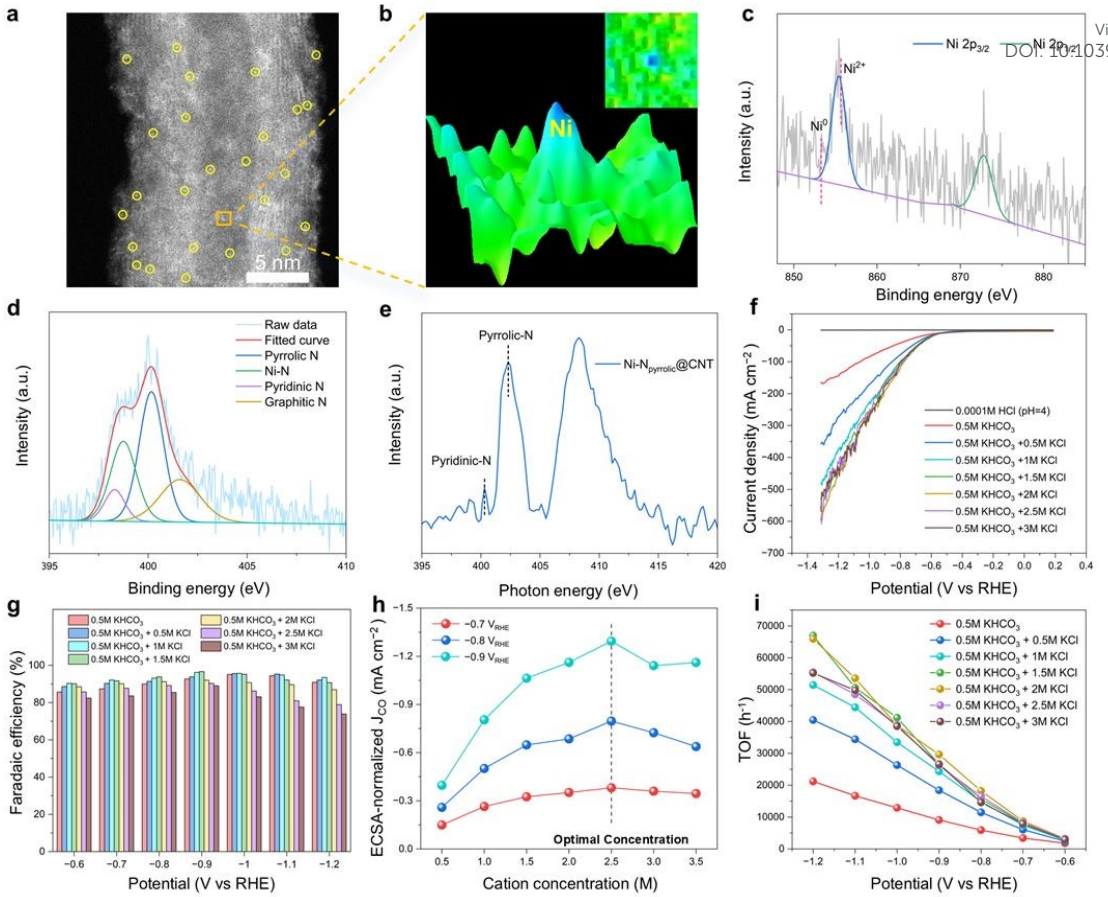

Fig. 5 (a) AC-HAADF-STEM images of Ni-$N_{pyrrolic}$@CNT. (b) 3D surface plot highlighting Ni sites. (c) Ni 2p XPS spectra. (d) N 1s XPS spectra. (e) Soft XAS of N K-edge. (f) LSV curves in electrolytes with different K^+ concentrations. (g) Faradaic efficiency of CO. (h) ECSA-normalized J_{CO} versus K^+ concentration. (i) TOF value under different K^+ concentrations.

free-energy barrier for CO desorption increases with increasing K^+ concentration. This trend originates primarily from the strengthened interaction between *CO and the Ni active site, as evidenced by the COHP analysis of the Ni-C(*CO) bond (Fig. S24). To further clarify whether the overall CO_2RR kinetics would continue to improve at higher cation concentrations, we extended the concentration range to $4K^+$ and investigated the corresponding reaction mechanism (Fig. S25−S28). As shown in Fig. S26, the formation of *COOH becomes more kinetically favorable in the $4K^+$ environment, with a reduced free-energy barrier of 0.35 eV. However, the free-energy barrier for *CO desorption increases to 0.48 eV (Fig. S28), exceeding that of *CO_2 hydrogenation. This shift indicates that, under the $4K^+$ condition, the rate-determining step changes from *CO_2 hydrogenation to *CO desorption. Notably, the *CO desorption barrier at $4K^+$ is also higher than the barriers of *COOH formation under $1K^+$, $2K^+$, and $3K^+$ conditions.

Fig. 4 summarizes the cation concentration-dependent free-energy barrier of each elementary step in the CO_2RR pathway. Based on the trend obtained through linear fitting, the difference of the free-energy barriers between *CO_2 hydrogenation and *CO desorption progressively decreases with increasing K^+ concentration. At a concentration between $3K^+$ and $4K^+$, the free-energy barriers for *COOH formation and *CO desorption become comparable. Beyond this point, *CO desorption overtakes CO_2 hydrogenation as the dominant rate-limiting step for CO_2RR on Ni-N-C SACs, suggesting that excessive cation concentration would ultimately impede overall CO_2RR kinetics. Overall, we can conclude that for CO_2RR, a higher K^+ concentration is not necessarily better, but rather there exists an optimal K^+ concentration before electrolyte saturation, at which the overall reaction kinetics reach their maximum. It should be specified here that the calculated free-energy barriers are used primarily to identify relative changes in reaction kinetics and rate-limiting behavior, rather than to provide quantitatively exact activation energies under operating electrochemical conditions.

Our results are consistent with the Sabatier principle[33] as the cation concentration can be linearly translated into the strength of the catalyst-adsorbate interactions, based on the clear linear relationship observed between ICOHP values and cation concentration (Fig. S29). Although our DFT/AIMD model does not explicitly include all aspects of the electrochemical environment, such as anions, potential-dependent double-layer structure, long-range space-charge effects, or local pH gradients, the systematic promotion of CO_2 reduction kinetics with increasing local K^+ concentration arising from stabilization of reaction intermediates and modification of the interfacial

environment—relies on relative trends that are expected to be robust.

Experimental Validation of the Existence of an Optimal Cation Concentration.

To verify whether there is indeed an optimal cation concentration for Ni-N-C SACs in catalyzing CO_2RR, we experimentally prepared Ni-N-C SACs and evaluated their catalytic performance over a wide range of K^+ concentrations. Firstly, nickel tetraphenylporphyrin (NiTPP) molecules were loaded onto acid-treated carbon nanotubes (CNTs), followed by precise pyrolysis, resulted in the synthesis of Ni sites-containing SACs (Ni-Npyrrolic@CNT, Fig. S30). In the XRD pattern (Fig. S31), the diffraction peaks of the (102) crystal plane of CNTs and the (111) crystal plane of metallic Ni overlap significantly, indicating that the formation of nickel nanoclusters or nanoparticles cannot be excluded. To resolve this ambiguity, we further employed aberration-corrected high-angle annular dark-field scanning transmission electron microscopy (AC-HAADF-STEM) for detailed characterization at the atomic resolution level. As shown in Fig. 5a, isolated bright spots are scattered across the CNTs surface, confirming atomic-level Ni dispersion and the absence of nanoclusters. A three-dimensional surface plot further visualizes the precise locations of Ni atoms (Fig. 5b). Energy-dispersive X-ray spectroscopy (EDS) mapping provides additional evidence for the uniform distribution of Ni and N atoms on the CNTs surface (Fig. S32). In addition, the Ni 2p X-ray photoelectron spectroscopy (XPS) spectra (Fig. 5c) show that the Ni 2p3/2 peak is close to the Ni^{2+} peak, while the absence of the Ni0 peak supports the conclusion of atomically dispersed Ni. The N 1s spectrum reveals four types of nitrogen: pyrrolic N, Ni-N, pyridinic N, and graphitic N (Fig. 5d). Among these, pyrrolic N and Ni-N dominant, indicating that controlled pyrolysis significantly preserves the coordination environment of Ni atoms within NiTPP molecules. Furthermore, soft X-ray absorption spectroscopy (XAS, Fig. 5e) at the N K-edge demonstrates that most nitrogen exists in the pyrrolic form. Overall, the above results demonstrate that we have successfully prepared Ni-N-C SACs featured with pyrrolic N atoms. In the Ni-$N_{pyrrolic}$@CNT, the Ni and N content are 0.59 wt% and 2.49 wt%, respectively. The BET surface area is 146.4 m^2/g (Fig. S33), and it contains mesopores with an average pore diameter of 21.5 nm, which may be a three-dimensional pore structure formed by the intertwining of carbon nanotubes.

KCl solutions of varying molarities were then introduced into a neutral electrolyte (0.5 M $KHCO_3$) to test the effect of K^+ concentration on electrocatalytic performance of as-obtained Ni-$N_{pyrrolic}$@CNT toward CO_2RR. As shown in Fig. 5f, when the KCl concentration increased from 0 to 1.5 M, the cathodic current increases sharply to several hundred mA. As the KCl concentration continues to rise beyond this point, the cathode current reaches a plateau. with the products consisting primarily of CO and H_2. As the KCl concentration increased to 1.5 M, CO efficiency continuously improved between −0.6 and −0.9 V_{RHE} (Fig. 5g). Further increases in K^+ concentration promoted hydrogen evolution, indicating that regulating K^+ within an optimal concentration range (0–1.5M) not only accelerates overall kinetic but also enhances CO selectivity. The electrochemical surface area (ECSA)-normalized current density (Fig. S34 and S35) for CO production (J_{CO}) as a function of cation concentration is shown in Fig. 5h. As the K^+ concentration increases from 0.5 M to 2.5 M, the ECSA-normalized J_{CO} exhibits a steady increase, indicating that elevated cation concentrations enhance reaction kinetics. However, when the K^+ concentration exceeds 2.5 M, a decline in J_{CO} is observed, suggesting an inhibitory effect at higher concentrations. This adverse trend becomes more pronounced at more negative potentials. The turnover frequency (TOF) values showed a similar growth trend, further demonstrating the crucial role of K^+ in accelerating reaction kinetics (Fig. 5i). Overall, the experimental results are in excellent agreement with the theoretical predictions, revealing a volcano-type dependence of CO production activity on cation concentration and confirming the existence of an optimal K^+ concentration for maximizing CO_2RR performance.

Conclusions

In summary, by means of constant-potential AIMD simulations, we comprehensively explored the effect of K concentration on the reaction kinetics of CO_2RR over Ni-N-C SACs. Our theoretical results reveal that K^+ concentration plays a pivotal role in stabilizing and activating adsorbed $^*CO_2$ by transferring more electrons. Further mechanistic simulations indicate that the kinetic process of $^*CO_2$ protonation to *COOH is more sensitive to changes in K+ concentration, enabling the pristine rate-determining step to be overcome. However, the gradually enhanced Ni–C bond with K^+ concentration makes $^*CO$ desorption kinetically unfavorable, which will replace $^*COOH$ formation as the new rate-determining step. As a result, excessively increasing the K^+ concentration can become counterproductive for CO_2RR, which indicates the presence of an optimal K^+ concentration that balances the reaction kinetics for $^*COOH$ formation and *CO desorption. The cation concentration-dependent reaction kinetics is further supported by the experimentally measured partial current density of CO production. Our findings redefine the role of electrolyte composition by identifying cation concentration as a previously overlooked but general kinetic descriptor, and they establish a new paradigm for electrolyte engineering in CO_2RR and other electrocatalytic reactions.

Methods

DFT Computations and Models. All atomic-scale simulations were performed by the Vienna Ab Initio Simulation Package (VASP) code with the projector augmented wave pseudopotential based on density functional theory (DFT).[34,35] The revised Perdew-Burke-Ernzerhof (RPBE) functional was employed to describe the exchange-correlation interactions within the generalized gradient approximation (GGA).[36,37] The kinetic energy cutoff of the plane wave was set to be 400 eV, and the convergence criterion for the residual forces and total energies were set to be 0.05 eV $Å^{-1}$ and 10^{-5} eV,

respectively. Bader charge calculation was performed to analyze the charge population and charge transfer.[38] The integrated crystal orbital Hamilton population (ICOHP) was employed to evaluate the strength of the Ni-C bond.[39] The empirical correction in Grimme's method (DFT+D3) was used to describe the van der Waals interactions.[40] The water/Ni-N-C interface was constructed using 80 explicit water molecules (average density ~1 g cm^{-3}) on a rectangular Ni-N-C configuration containing 62 carbon atoms, 4 nitrogen atoms, 1 nickel atom, and 8 hydrogen atoms. The cell size of the models is 17.22 × 12.78 × 28 $Å^3$, with a 15 Å-vacuum region along the z-direction to prevent interactions between the periodic slabs. A Gamma-centered k-point mesh was employed to sample the Brillouin zone.[41] Different amounts of potassium ions (K^+) were introduced into the explicit water layer to simulate varying cation concentrations.

Molecular Dynamics Simulations. Constant-potential *ab initio* molecular dynamics (AIMD) simulations were performed using CP-VASP,[42,43] which determines the target electrode potential based on the Fermi level that fluctuates with the number of electrons in the system. The implicit solvent environment was simulated by the VASPsol code,[44] which treats the electrode-electrolyte interface as a polarizable continuum and places ionic counter-charges at the interface to maintain system electroneutrality. The canonical ensemble (NVT) was imposed by a Nose-Hoover thermostat at 300 K,[45,46] and the electrode potential was preset to −0.7 V_{RHE} for the equilibrium AIMD simulations. A 1.2 fs time step is used in AIMD simulations with the hydrogen mass set to 2 atomic mass units.[47,48] A standard AIMD simulation of 10 ps was performed at 300 K to allow the solvation structures of cations to reach the relative equilibrium state for subsequent reaction kinetic calculations. Free energy profile was obtained via the thermodynamic integration within the constrained molecular dynamic framework (*i.e.*, the slow-growth approach combined with the bule-moon ensemble). The increment of the collective variable (CV) was set to 0.0003 Å/step for the transition state search process.

In CP-VASP, the electrode potential (Uq) referenced to the standard hydrogen electrode (SHE) scale is defined as:

$$U_q(\text{V vs. SHE}) = \Phi_{SHE} - \Phi_q/e \quad (1)$$

where Φ_q is the electron energy, and Φ_{SHE} is the absolute potential of the SHE, which is set to −4.6 V in this work.

Based on the experimental pH value of 6.8 (0.5 M $KHCO_3$), we converted the electrode potentials to the reversible hydrogen electrode (RHE) scale in all constant potential computational procedures using the following formula:

$$U_q(\text{V vs. RHE}) = U_q(\text{V vs. SHE}) + k_BT \times \ln 10 \times 6.8 \quad (2)$$

Reagent and Materials. Nickel tetraphenylporphyrin (NiTPP), Potassium hydroxide (KOH), Glycerol, N,N-Dimethylformamide (DMF) and Ethanol were obtained from Aladdin. Multi-walled carbon nanotubes (CNTs, purity >95%, length ~50 μm and product number: 100240) was obtained from Xianfeng Nano. Nafion perfluorinated resin solution (5 wt% in lower aliphatic alcohols and water, contains 15-20% water) was obtained from Sigma-Aldrich. All the reagents were used as received without further purification. Deionized water was used throughout this study.

Pre-Treatment of CNTs. 500 mg of CNT was dispersed in a beaker containing 49.5 mL of water and 49.5 mL of ethanol. Subsequently, 9 mL of HCl was added, and the mixture was sonicated for 30 minutes. It was then stirred and heated at 60°C for 6 hours. Finally, the mixture was centrifuged and washed with deionized water until pH ≈ 7.0.

Experimental synthesis of Ni-Npyrrolic@CNT. 70 mg of CNTs was dispersed in a solution containing 70 mL DMF by sonication for 30 min (solution A). Then, 70 mg of NiTPP was dispersed in a solution containing 140 mL DMF by sonication for 30 min (solution B). Solution B was then added slowly into solution A with continuous sonication for 30 min. The mixed solution was magnetically stirred for 24 hours at room temperature, after which it was centrifuged and washed twice with DMF, water and ethanol, respectively. Finally, the product is collected for future use after being freeze-dried for 24 hours. Then, the product was placed in a tube furnace, heated under Ar gas protection at a rate of 2 ℃/min to 460 ℃ and then kept for 2 h, after which they were naturally brought to room temperature. The resulting samples are referred to as Ni-$N_{pyrrolic}$@CNT.

Characterizations. Powder X-ray diffraction patterns of samples were recorded on a Rigaku Miniflex-600 with Cu Kα radiation (Cu Kα, λ = 0.15406 nm, 40 kV and 15 mA). TEM images were recorded using a Hitachi-7650 worked at 100 kV. The high-resolution TEM, HAADF-STEM were recorded by a FEI Tecnai G2F20 S-Twin high-resolution transmission electron microscope working at 200 kV, on a JEOL JEM-ARM200F TEM/STEM with a spherical aberration corrector working at 200 kV. X-ray photoelectron spectroscopy (XPS, VG-Multilab2000) was performed by using Al Kα radiation (1486.71 eV). The gas chromatographs (PANNA A91) equipped with a TCD and FID detector is used to detected the generated gas. Liquid NMR were quantified by the Bruker AVANCE III 400MHZ using dimethyl sulfoxide as an internal standard. The specific surface area of the materials was measured using a specific surface area analyzer (ASAP 2460), and the elemental composition of the materials was analyzed using an inductively coupled plasma emission spectrometer (Agilent 725-ES).

Data availability

The authors declare that the data supporting the findings of this study are available within the paper and its supplementary information files.

Author Contributions

Y. L. advised and supervised the work. L.K. and Z.C. conceived the idea and designed the simulations. L.K. performed the whole DFT calculations. Y C. participated in part of the analysis of the AIMD simulations. L.W. worked on material characterizations and electrocatalysis experiments. Y.W. commented on the paper. All authors discussed and commented on the manuscript.

Conflicts of interest

The authors declare no competing financial interests.

View Article Online
DOI: 10.1039/D5SC09270J

Acknowledgements

The authors are grateful for funding support from the National Key R&D Program of China (2024YFA1210804 and 2024YFA0917802), the National Natural Science Foundation of China (Nos. 22425302, and 22203044), and the Priority Academic Program Development of Jiangsu Higher Education Institutions.

References

1 L. Li, X. Li, Y. Sun and Y. Xie, *Chem. Soc. Rev.*, 2022, **51**, 1234-1252.
2 M. B. Ross, P. De Luna, Y. Li, C.-T. Dinh, D. Kim, P. Yang and E. H. Sargent, *Nat. Catal.*, 2019, **2**, 648-658.
3 S. Overa, B. H. Ko, Y. Zhao and F. Jiao, *Acc. Chem. Res.*, 2022, **55**, 638-648.
4 P.-P. Yang and M.-R. Gao, *Chem. Soc. Rev.*, 2023, **52**, 4343-4380.
5 S. Nitopi, E. Bertheussen, S. B. Scott, X. Liu, A. K. Engstfeld, S. Horch, B. Seger, I. E. Stephens, K. Chan and C. Hahn, *Chem. Rev.*, 2019, **119**, 7610-7672.
6 M. Li, H. Wang, W. Luo, P. C. Sherrell, J. Chen and J. Yang, *Adv. Mater.*, 2020, **32**, 2001848.
7 S. Zhao, R. Jin and R. Jin, *ACS Energy Lett.*, 2018, **3**, 452-462.
8 X. Su, X.-F. Yang, Y. Huang, B. Liu and T. Zhang, *Acc. Chem. Res.*, 2018, **52**, 656-664.
9 S. Liang, L. Huang, Y. Gao, Q. Wang and B. Liu, *Adv. Sci.*, 2021, **8**, 2102886.
10 A. S. Varela, W. Ju, A. Bagger, P. Franco, J. Rossmeisl and P. Strasser, *ACS Catal.*, 2019, **9**, 7270-7284.
11 X. Li, W. Bi, M. Chen, Y. Sun, H. Ju, W. Yan, J. Zhu, X. Wu, W. Chu and C. Wu, *J. Am. Chem. Soc.*, 2017, **139**, 14889-14892.
12 H. B. Yang, S.-F. Hung, S. Liu, K. Yuan, S. Miao, L. Zhang, X. Huang, H.-Y. Wang, W. Cai and R. Chen, *Nat. Energy*, 2018, **3**, 140-147.
13 Z. Huang, T. Yang, Y. Zhang, C. Guan, W. Gui, M. Kuang and J. Yang, *Chin. J. Catal.*, 2024, **63**, 61-80.
14 H. Khani, A. R. Puente Santiago and T. He, *Angew. Chem. Int. Ed.*, 2023, **62**, e202306103.
15 Y. Xu, Z. Xia, W. Gao, H. Xiao and B. Xu, *Nat. Catal.*, 2024, **7**, 1120-1129.
16 W. Ren, A. Xu, K. Chan and X. Hu, *Angew. Chem. Int. Ed.*, 2022, **61**, e202214173.
17 Q. Wu and Z. J. Xu, *Angew. Chem. Int. Ed.*, 2025, **64**, e202505022.
18 J. Resasco, *JACS Au*, 2025, **5**, 5253-5266.
19 K. Ye, Y. Han, F. Wu, X. Cheng, Z. Duan, G. Zhang, P. Hu and M. S. Ahlquist, *ACS Catal.*, 2025, **15**, 17672-17677.
20 A. Malkani, J. Li, N. Oliveira, M. He, X. Chang, B. Xu and Q. Lu, *Sci. Adv.*, 2020, **6**, eabd2569.
21 J. Resasco, L. D. Chen, E. Clark, C. Tsai, C. Hahn, T. F. Jaramillo, K. Chan and A. T. Bell, *J. Am. Chem. Soc.*, 2017, **139**, 11277-11287.
22 A. J. King, J. C. Bui, A. Z. Weber and A. T. Bell, *ACS Catal.*, 2025, **15**, 14588-14600.
23 F. Wu, X. Liu, S. Wang, L. Hu, S. Kunze, Z. Xue, Z. Shen, Y. Yang, X. Wang and M. Fan, *Nat. Commun.*, 2024, **15**, 6972.
24 H. Yun, S. Yoo, J. Son, J. H. Kim, J. Wu, K. Jiang, H. Shin and Y. J. Hwang, *Chem*, 2025, **11**, 102461.
25 T. Möller, W. Ju, A. Bagger, X. Wang, F. Luo, T. N. Thanh, A. S. Varela, J. Rossmeisl and P. Strasser, *Energy Environ. Sci.*, 2019, **12**, 640-647.
26 Z. Chen, J. Liu, J. Li, Y. Zhang, J. Yang, J. Li, Z. Wang, Z. Liu and S. Q. Zang, *Angew. Chem. Int. Ed.*, 2025, **64**, e202506845.
27 R. Boppella, M. Austeria P, Y. Kim, E. Kim, I. Song, Y. Eom, D. P. Kumar, M. Balamurugan, E. Sim and D. H. Kim, *Adv. Funct. Mater.*, 2022, **32**, 2202351.
28 Q. Song, B. Guo, H. Liu, H. Wang, M. Schmidt, P. A. van Aken, D. Luo and E. Klemm, *Cell Rep. Phys. Sci.*, 2023, **4**, 101737.
29 X. Zhao and Y. Liu, *J. Am. Chem. Soc.*, 2020, **142**, 5773-5777.
30 Y. Cui, C. Ren, Q. Li, C. Ling and J. Wang, *J. Am. Chem. Soc.*, 2024, **146**, 15640-15647.
31 Y. Han, Y. Wei, A. Goswami and A. Alexandrova, *J. Am. Chem. Soc.*, 2025, **147**, 38636-38646.
32 Y. Wang, L. You and K. Zhou, *Chem. Sci.*, 2021, **12**, 14065-14073.
33 A. J. Medford, A. Vojvodic, J. S. Hummelshøj, J. Voss, F. Abild-Pedersen, F. Studt, T. Bligaard, A. Nilsson and J. K. Nørskov, *J. Catal.*, 2015, **328**, 36-42.
34 G. Kresse and J. Furthmüller, *Phys. Rev. B*, 1996, **54**, 11169.
35 P. E. Blöchl, *Phys. Rev. B*, 1994, **50**, 17953.
36 B. Hammer, L. B. Hansen and J. K. Nørskov, *Phys. Rev. B*, 1999, **59**, 7413.
37 J. P. Perdew, K. Burke and M. Ernzerhof, *Phys. Rev. Lett.*, 1996, **77**, 3865.
38 G. Henkelman, A. Arnaldsson and H. Jónsson, *Comput. Mater. Sci*, 2006, **36**, 354-360.
39 R. Dronskowski and P. E. Blöchl, *J. Phys. Chem.*, 1993, **97**, 8617-8624.
40 L. Goerigk and S. Grimme, *Phys. Chem. Chem. Phys.*, 2011, **13**, 6670-6688.
41 H. J. Monkhorst and J. D. Pack, *Phys. Rev. B*, 1976, **13**, 5188.
42 X. Zhao and Y. Liu, *J. Am. Chem. Soc.*, 2021, **143**, 9423-9428.
43 S. Yu, Z. Levell, Z. Jiang, X. Zhao and Y. Liu, *J. Am. Chem. Soc.*, 2023, **145**, 25352-25356.
44 K. Mathew, V. C. Kolluru, S. Mula, S. N. Steinmann and R. G. Hennig, *J. Chem. Phys.*, 2019, **151**, 234101.
45 S. Nosé, *J. Chem. Phys.*, 1984, **81**, 511-519.
46 W. G. Hoover, *Phys. Rev. A*, 1985, **31**, 1695.
47 T. Cheng, H. Xiao and W. A. Goddard III, *Proc. Natl. Acad. Sci. U.S.A.*, 2017, **114**, 1795-1800.
48 Y. Li and Z.-F. Liu, *J. Phys. Chem. Lett.*, 2021, **12**, 6448-6456.

View Article Online
DOI: 10.1039/D6SC03277J

The authors declare that the data supporting the findings of this study are available within the paper and its supplementary information files.